Revision 2

Representative size distributions of framboidal, euhedral and sunflower pyrite from high-resolution X-ray tomography and scanning electron microscopy analyses

Raul Merinero[1,*], Víctor Cárdenes[2], Rosario Lunar[1,3], Matthieu N. Boone[2], Veerle Cnudde[2]

[1] Department of Crystallography and Mineralogy, Complutense University of Madrid, C/ Jose Antonio Novais, 2, 28040 Madrid, Spain

[2] PProGRess-UGCT Department of Geology, Ghent University, Krijgslaan 281 (S8), 9000 Ghent, Belgium

[3] Geosciences Institute, Department of Crystallography and Mineralogy, Complutense University of Madrid, C/ Jose Antonio Novais, 2, 28040 Madrid, Spain

[4] Radiation Physics-UGCT Department of Physics and Astronomy, Ghent University, Poeftuinstraat 86 (N12), 9000 Ghent, Belgium

*E-mail: rmeriner@ucm.es

Abstract

A statistical procedure designed to obtain representative size distributions for different morphologies and arrangements of pyrite is described here. This statistical procedure is applied to data acquired during scanning electron microscopy (SEM) and high-resolution X-ray tomography (micro-CT) analyses. The statistical procedure was tested in methane-derived carbonate pipes recovered in the Gulf of Cadiz. These samples contain abundant pyrite together with pseudomorph iron oxyhydroxides showing multiple morphologies including euhedral crystals, framboids and sunflowers (framboidal core with outer crystals).

The SEM analysis consisted in the establishment of independent populations of pyrite and iron oxyhydroxides grouped by morphology and arrangement and the determination of its size distributions. Micro-CT analysis included a determination of the 3D volume of pyrite from the density difference between pyrite and the rest of mineral forming the samples. The use of the micro-CT technique implies that minerals with similar attenuation coefficients than those of pyrite are scarce or not present in the studied samples. A filtering process was applied to the 3D volume. This filtering process consisted of the selection of objects with corrected sphericity greater than 0.80, discrete compactness greater than 0.60, elongation and flatness of the circumscribed 3D ellipsoid less than 1.80 and the sum of the elongation and flatness less than 3. Objects with shapes similar to those expected in pyrite (spheroidal and regular shapes) were selected with this filtering process. The optimal mixture of lognormal size distributions was obtained applying statistical techniques to the entire size distribution represented by the filtered objects. The correspondence between size distributions obtained during the SEM and the micro-CT analyses was done by matching statistical parameters and using 3D renderings. The representative size distributions of pyrite as determined by the proposed 3D processing methodology can be used to accurately quantify the paleo-environmental conditions of pyrite formation, which would solve some of the limitations resulting from analyses based on 2D images.

Keywords: pyrite, size distributions, framboids, euhedrae, sunflowers, micro-CT

Introduction

Framboids are defined as microscopic, spheroidal clusters of densely packed homogeneous microcrystals (Ohfuji and Rickard 2005). The most common mineralogical components of framboids are iron sulfides, such as pyrite. Under sedimentary conditions they are formed in the vicinity of the sediment-water interface

(Wilkin et al. 1996). They are also very frequent in pyrite formed within methane-derived carbonates in marine cold-seeps (Peckmann and Thiel 2004). In these environments, framboidal pyrite is formed by the reaction between H_2S, produced by the activity of sulfate reduction bacteria (SRB), and detrital Fe minerals. In the SRB-mediated environments, euhedral crystals and other morphologies of pyrite usually occur in close conjunction with framboidal pyrite (e.g. Merinero et al. 2009; Cavalazzi et al. 2012; Wang et al. 2013; Gallego-Torres et al. 2015). The coexistence of framboidal and euhedral pyrite has been attributed to the early formation of framboidal pyrite under conditions of FeS_2 supersaturation and the subsequent decrease in FeS_2 saturation by the exhaustion of sources of highly reactive Fe or the decrease in SRB activity (Cavalazzi et al. 2012). This decrease in FeS_2 saturation promotes the growth of microcrystals to form euhedral crystals instead of framboidal pyrite (Butler and Rickard 2000) or the overgrowth and recrystallization of framboidal pyrite that evolves into euhedral pyrite (Sawlowicz 1993). The existence of other morphologies of pyrite such as sunflower pyrite (framboidal core with outer crystals) has been explained as the results of the evolution from framboidal to euhedral pyrite (e.g. Merinero et al. 2008) although the role of sunflowers in the whole process has not been detailed. Few works refer to pyrite with internal framboidal texture and external regrowth as sunflower pyrite (e.g. Large et al. 1999). Wilkin et al. (1996) described the infilling of interstitial voids in framboidal pyrite leading to the “welded sphere” morphology previous to the formation of the external overgrowth. Authors also use the terms “framboidal pyrite with overgrowths” (Ding et al. 2014) or “overgrowth crystals upon framboids” (Wei et al. 2012). In all cases, this morphology represented the continuation of the growth of framboids without incorporating new microcrystals into the framboidal texture but instead with the overgrown of prismatic pyrite under conditions other than supersaturation (Suits and Wilkin 1998).

The diameter of authigenic framboidal pyrite ranges generally from 5 to 20 μm, and the size of the component microcrystals is usually less than 2 μm, although framboids up to 250 μm have been reported (Ohfuji and Rickard 2005). Based on the work of Wilkin et al. (1996), the size distribution of small framboidal pyrite has been used to infer the palaeoconditions (e.g., Wignall et al. 2005; Bond and Wignall 2010; Liao et al. 2010; Wang et al. 2013; Guan et al. 2014; Tian et al. 2014; Takahashi et al. 2015; Wei et al. 2015). Moreover, the size distribution of framboidal and euhedral pyrite can be used to establish the history and conditions of the nucleation and growth of pyrite (e.g. Pósfai et al. 2001; Merinero et al. 2009). Up to now, the size distribution of microscopic pyrite has been determined from direct observation of thin sections under optical microscopy (e.g. Ding et al. 2014; Blood and Lash 2015) and from 2D photomicrographs obtained through SEM (e.g. Wei et al. 2012, 2015; Guan et al. 2014). These techniques have some limitations, such as the lack of representativeness, the underestimation of the small sizes and the imprecision of measurement in random cuts through the microscopic pyrite, resulting in size distributions with possibly significant errors. One still outstanding issue to follow up on is whether the smaller framboids are actually underestimated, in terms of their number in population distributions. Recently, representative size distributions of microscopic pyrite occurring in shales have been calculated from 3D representations obtained using micro-CT (Cárdenes et al. 2016).

The goal of this paper is to develop a statistical procedure that obtains representative size distributions of pyrite grouped by morphology and arrangement based on SEM and micro-CT analysis of geologic samples. This statistical procedure was tested here in methane-derived carbonate pipes that contain abundant pyrite and pseudomorph iron oxyhydroxides. Pyrite and iron oxyhydroxides show different morphologies and arrangement including framboids, euhedrae and sunflowers.

Experimental and analytical methods

Samples

The carbonate pipes studied here were collected on the Iberian continental margin of the Gulf of Cadiz during the oceanographic cruises Anastasya 2001, ARSA 0309 and INDEMARES/CHICA 0211, aboard the research vessel Cornide de Saavedra. More than 400 carbonate pipes were recovered from the seafloor during these cruises at depths ranging from 700 to 1100 m using rectangular, benthic-type dredges (Díaz-del-Río et al. 2003, Rueda et al. 2012; Vila et al. 2013). Mineralogy and textures of the carbonate pipes were previously studied showing the presence of pyrite and several unidentified iron oxyhydroxide phases (Díaz-del-Río et al. 2003, Merinero et al. 2008).

Four samples were selected based on the morphologies of pyrite and iron oxyhydroxides. For two of them, the outer and inner parts of the sample were studied separately (Fig. 1). The nomenclature of the samples used in this study is summarized in Table 1.

Scanning Electron Microscopy (SEM) analysis

Thin sections (transversal and longitudinal views) of the carbonate pipes were studied in detail under optical microscopy and SEM. The SEM analysis determined the size distribution of pyrite and iron oxyhydroxides grouped by morphology and arrangement. Observations and photomicrographs were performed in back scattered imaging mode with a JEOL Superprobe JXA-8900M at the National Center for Electron Microscopy (Complutense University of Madrid) with a voltage of 20 kV and a current intensity of 50 nA. Sizes were calculated from photomicrographs obtained with the JEOL

Superprobe following the method used by Merinero et al. (2009) and using ImageJ 1.50b software (Schneider et al. 2012).

High resolution X-ray computed tomography (micro-CT) analysis

Micro-CT is a 3D visualization and measurement technique in which the object being studied is represented as a discretized 3D volume of the local linear X-ray attenuation coefficient. From this 3D volume it is possible to estimate the size distribution of minerals with X-ray linear attenuation coefficients different than those of their matrix and of surrounding minerals (Cnudde and Boone 2013). Here we use this technique to estimate the entire size distribution of the pyrite and iron oxyhydroxides.

We obtained cylindrical samples 4 mm in diameter and 10 mm in length from each sample for analysis with micro-CT. These cylindrical samples were scanned with the HECTOR setup (Masschaele et al. 2013), located at the Center for X-ray Tomography at Ghent University (www.ugct.ugent.be). A high voltage of 130 kV and a tube power of 10 W were used for the measurements, with a 1 mm aluminum filter in order to reduce the beam-hardening effect (Cnudde and Boone 2013). More than 1800 projections of each sample were obtained during a complete rotation along a vertical axis, achieving a voxel size of 2.5 μm. The projections obtained by micro-CT were reconstructed using Octopus software (Vlassenbroeck et al. 2007). The reconstructed images were analyzed with ImageJ 1.50b software (Schneider et al. 2012). Firstly, reconstructed images were converted from 16 to 8 bits per pixel and filtered using the median filter function of the ImageJ plugin 3D Fast Filters (Ollion et al. 2013). Subsequently, individual mineral objects representing pyrite or iron oxyhydroxides were 3D-segmented according to their grey-scale values using the ImageJ plugin RoiManager3D 2.0 (Ollion et al. 2013). For each object, we measured the following parameters: volume (μm^3), surface (μm^2) and 3D ellipsoid circumscribed to the object (major, intermediate and minor radii in μm). The longest diameter of the 3D ellipsoid was considered as the size of the analyzed object. For each object the following parameters were estimated: classical sphericity ψ (Wadell 1935), corrected sphericity ψ_c (Lindblad 2005) and discrete compactness C_d (Bribiesca 2008):

$$\Psi = \frac{\pi^{\frac{1}{3}}(6V_p)^{\frac{2}{3}}}{A_p};\ \Psi_C = \frac{\pi^{\frac{1}{3}}(6V_p)^{\frac{2}{3}}}{A_C};\ C_d = \frac{V_p - \frac{A_p}{6}}{V_p - \left(\sqrt[3]{V_p}\right)^2}$$

Where V_p and A_p are the measured volume and surface of the object and A_c is the corrected surface estimated from the algorithm developed by Lindblad (2005). Elongation and flatness of the circumscribed 3D ellipsoid were calculated from the ratio between the major and the intermediate radii and the intermediate and minor radii respectively. Finally, 3D renderings of individual objects were performed using the plugin RoiManager3D 2.0 (Ollion et al. 2013).

A filtering process was applied to the segmented 3D objects to select exclusively regular and spheroidal objects. The filtering process was divided into 4 steps (Table 2). The first step consisted of the adjustment to the theoretical lognormal distribution in the smaller sizes. During steps 2, 3 and 4, objects with different shapes than those expected for pyrite and iron oxyhydroxides (framboidal, euhedral or sunflower) were removed on the basis of to their corrected sphericity, discrete compactness, elongation and flatness of the circumscribed 3D ellipsoid (Table 2).

Statistical analysis

Data management and analysis were performed using the statistical software R v. 3.2.3 (R_Core_Team 2015). Lognormality of the size populations obtained from the SEM analysis was assessed by quantile-quantile plots and applying the Shapiro-Wilk test of normality (Royston 1995) to the natural logarithm of the size. Mixture of lognormal populations was analyzed from the entire size distribution obtained from the micro-CT analysis and the four-step filtering process. The Mclust function of the R package mclust v. 4.4 (Fraley and Raftery 2002; Fraley et al. 2012) was used to estimate the optimum mixture modelling of lognormal populations fitted via an expectation-maximization algorithm including Bayesian regularization and dimension reduction. The Mclust function gives the parameters of the independent lognormal populations (mean, standard deviation and proportion in the entire size distribution) together with the probability that each individual object belongs to one or another population. The percentage in volume was obtained multiplying this probability by the individual volume of each object. The minimum and maximum of the independent lognormal populations were estimated from the size of those objects with probability of belonging to that population greater than 0.10.

Results

Carbonate pipes consist of microcrystalline carbonate (Fe-rich dolomite, ankerite and Mg-rich calcite) containing well-preserved detrital grains of quartz and foraminiferal shells and minor phyllosilicates, k-feldspars, apatite and Fe-Ti-oxides. Pyrite and pseudomorph iron oxyhydroxides are commonly found in the void spaces resulting from primary and secondary porosity. The main morphologies of pyrite and iron oxyhydroxides are framboids, euhedrae and sunflowers (Fig. 2). In the Cornide sample, pyrite is totally transformed into iron oxyhydroxides. In the Hespérides, Almazán outer and inner samples, pyrite is partially transformed into iron oxyhydroxides. In the DIASOM outer and inner samples, pyrite is preserved and transformation into iron oxyhydroxides is not observed.

SEM analysis

The focus of the SEM analysis of the carbonate pipes was on the morphology and arrangement of the iron minerals, which allowed us to establish independent populations based on these features. Groups of specimens with spheroidal shape were also considered as independent populations. Size distribution was calculated for each population and represented in histograms.

In the Cornide sample, iron oxyhydroxides are disseminated in the matrix and associated with the infilling of small fractures (Fig. 3a). Disseminated iron oxyhydroxides show euhedral morphologies (Figs. 3a and 3b). In the fractures, iron oxyhydroxides have sunflower morphologies (Figs. 3a and 3c). The larger objects preserve the features of the sunflower morphology (Fig. 3c). The smaller objects show euhedral shapes, preserving some internal features of the sunflower morphology and showing dark inclusions (Fig. 3c). Groups of several objects with sunflower morphologies are common and some of them have regular shapes (Fig. 3b).

In the Hespérides sample, pyrite and iron oxyhydroxides occur in association with the infilling of small fractures, disseminated in the matrix and inside foraminiferal shells (Fig. 3d). Pyrite and iron oxyhydroxides with euhedral, framboidal and sunflower morphologies are observed. Two types of euhedral morphologies can be distinguished: disseminated in the matrix (euhedral-1, Figs. 3d and 3e) and in close proximity to framboids (euhedral-2, Figs. 3d and 3f). Disseminated euhedral crystals are of smaller size than those in close proximity to framboids. Framboidal morphologies are observed inside foraminiferal shells (framboidal-1, Fig. 3d) and fractures (framboidal-2, Fig. 3f), although infillings of foraminiferal shells are very scarce. Sunflower morphologies as individual or groups of specimens only occur in association with fractures (Fig. 3e).

The Almazán outer sample is characterized by the presence of individual euhedral crystals of pyrite disseminated in the matrix (euhedral-1, Figs. 3g and 3h) and groups of euhedral crystals infilling foraminiferal shells and small holes in the matrix (euhedral-2, Figs. 3h and 3i). Disseminated euhedral crystals are of smaller size than those forming groups. Individual framboids associated with the infilling of small fractures (framboidal-1, Figs. 3g and 3h) and groups of framboids formed inside foraminiferal shells (framboidal-2, Figs. 3g and 3i) are also common in this sample.

The Almazán inner sample is characterized by the existence of numerous holes and unfilled fractures and the absence of foraminiferal shells. Iron minerals are observed around these holes and present framboidal and euhedral morphologies (Figs. 4a, 4b and 4c). The formation of groups of framboids is very common in this sample (Fig. 4c).

In the DIASOM outer sample, pyrite is associated with the infilling of fractures and foraminiferal shells (Fig. 4d). Pyrite associated with the infilling of fractures shows both framboidal (Fig. 4e) and euhedral morphology (euhedral-1, Figs. 4d and 4f). Pyrite inside foraminiferal shells shows euhedral morphology (euhedral-2, Fig. 4f). In this sample, groups of framboids and foraminiferal shells with the chambers completely infilled are very common and therefore considered as an individual population of spheroidal shape (Figs. 4d and 4e).

The DIASOM inner sample is characterized by an abundance of pyrite infilling fractures and forming concretions of multiple specimens (Fig. 4g). Sunflower pyrite is the main morphology in this sample in close proximity to euhedral crystals with internal sunflower features (Figs. 4h and 4i). Foraminiferal shells are also abundant and are completely infilled with concretions of pyrite with internal framboidal features (Fig. 4i). Individual euhedral crystals are also present disseminated in the matrix (Fig. 4g).

The mean, standard deviation, minimum and maximum of the size of each individual population considered in the SEM analysis are included in Table 3, and histograms are plotted in the Fig. 5. Most of the histograms are mono-modal and have a lognormal shape (Fig. 5). The theoretical lognormal distribution fits on the mode in each population (Fig. 5). The quantile-quantile plots and the Shapiro-Wilk test applied to the natural logarithm of the size are also included in Fig. 5. Deviations from lognormality are observed in some populations of the smaller or larger sizes, although most of the populations can be considered lognormal.

Micro-CT and statistical analysis

The entire size distribution containing the mixture of independent populations of pyrite and iron oxyhydroxides was obtained during the micro-CT analysis and the four-step filtering process. The total number, mean, standard deviation, minimum and maximum sizes of the objects discarded in each step of the filtering process are summarized in Table 4. The histograms of the entire size distribution for each sample are represented in Fig. 6. The presence of multiple peaks in the histograms corresponding to multiple modes is the most significant feature. These peaks are more appreciable for the smaller sizes.

The optimal number of independent lognormal subpopulations forming the entire size distribution was obtained using the Mclust function. The mean, standard deviation, minimum, maximum, percentages in volume and number of objects for each independent lognormal subpopulation are summarized in Table 3. The probability density functions of each lognormal subpopulation obtained with Mclust are represented superposed over the histograms of the entire size distribution (Fig. 6). The modes of most of these lognormal subpopulations fit on the peaks obtained in the histograms (Fig. 6).

Discussion

Filtering process of the 3D objects and separation into independent subpopulations

Although micro-CT analysis provides statistically representative size distributions of minerals with different attenuation coefficients than the rest, there are several limitations that should be taken into account when it is applied to samples with abundant pyrite, and that the statistical procedure described here solves or minimize its impact:

- The presence of minerals with attenuation coefficients similar to those of pyrite or iron oxyhydroxides
- The presence of noise, affecting mostly to objects of smaller size
- The existence of groups of pyrite and iron oxyhydroxides not representing individual framboids, euhedrae or sunflowers
- The mixture of independent populations of pyrite and iron oxyhydroxides in the entire size distribution

Selection based on attenuation coefficients. The calculated linear attenuation coefficients for pyrite and iron oxyhydroxides are very different from those of the other main minerals in carbonate pipes, such as Fe-rich dolomite, ankerita, Mg-rich calcite and quartz (Fig. 7). This allows for easy differentiation of pyrite and iron oxyhydroxides from the carbonate matrix and clasts contained in the carbonate matrix. The linear attenuation coefficients for most of the accessory minerals—such as phyllosilicates (biotite-muscovite), k-feldspars and apatite—are also very different from those of pyrite and iron oxyhydroxides (Fig. 7). However, the linear attenuation coefficient of the Fe-Ti-oxides (also present in the carbonate matrix as clasts, though in less abundance) is similar to those of pyrite and iron oxyhydroxides. The irregular shape of the Fe-Ti-oxides is different from the spheroidal or regular shape of pyrite and iron oxyhydroxides. Because of the non-spheroidal shape of Fe-Ti-oxides, most of them were discarded during the four-step filtering process. Given the high number of objects obtained representing pyrite and iron oxyhydroxides (15000 objects on average), the inclusion of a few objects representing spheroidal Fe-Ti-oxides in the entire size distribution does not alter the statistical representativeness of the results obtained using micro-CT.

Noise filtering. Although the application of appropriate filtering to the micro-CT reconstructed images may reduce noise (Brabant et al. 2011), some will always persist. It is known that a significant number of smaller-size objects found in a sample can be noise (Cnudde and Boone 2013). Assuming that the size distributions of pyrite and iron oxyhydroxides were lognormal or quasi-lognormal, during the first step of the filtering process the entire size distribution was adjusted to the theoretical lognormal distribution at the smaller range of the size distribution, where noise is more of an issue.

Groups and selection of spheroidal objects. Micro-CT is effective to obtain significant size distributions when pyrite occurs as individual specimens (Cárdenes et al. 2016). However, when pyrite also forms groups it is impossible to separate individual objects from groups without additional manipulation of the images (Higgins 2000). In the carbonate pipes that we studied, pyrite usually forms multiframboidal textures and polyframboids (Merinero et al. 2008, 2009). Therefore, it is necessary to select only individual objects to obtain the real size distribution. Here, the selection of individual objects was done according to the sphericity, compactness, elongation and flatness of the objects, discarding objects with shapes to different than those expected (Table 2).

Classical sphericity is the most important shape factor for defining the roundness of an object. It varies from 0 to 1, where the maximum correspond to a perfect sphere and ranges from 0.8 to 1 for regular polyhedrons, such as cubes (0.806), regular octahedrons (0.846), dodecahedrons (0.910) or icosahedrons (0.939) the most common forms that pyrite takes. Therefore, objects representing framboids (spheroidal packing of microcrystals), euhedrae (isometric shapes) and sunflowers (framboidal core with outer crystals) should have a sphericity of greater than 0.8. When minerals are represented by discrete objects, the problem of classical sphericity is to estimate the surface area accurately. Classical sphericity uses the number of foreground voxels as surface area, but this measure is only effective for large objects (Lindblad 2005). Corrected sphericity uses the corrected surface based on the surface area estimation developed by Lindblad (2005) for discrete 3D objects and reduces the error for sphericity estimated in small objects. Therefore, during the second step of the filtering process (Table 2), objects with corrected sphericity less than 0.80 were discarded, which corresponded to large objects with mean size ranging from 48.95 to 103.6 μm (Table 4). With this criterion, large irregular groups of pyrite such as polyframboids were removed from the sample.

Corrected sphericity is sensitive to rotations and translations, but invariant with respect to the existence of holes in the object (Montero and Bribiesca 2009). An alternative shape descriptor for roundness is discrete compactness, an intrinsic characteristic of the shape of objects defined as the ratio between volume and area. Discrete compactness is invariant with respect to rotations and translations, but sensitive to the existence of holes; and objects with the same discrete compactness have similar shapes (Bribiesca 2008). Cubes and spheres have the greatest discrete compactness (1 and 0.99, respectively), and regular octahedrons and dodecahedrons usually have a discrete compactness greater than 0.60 (Bribiesca 2000). Therefore, objects with discrete compactness greater than 0.60 were selected during the third step (Table 2), including the expected shapes of pyrite. The mean size of the objects discarded in this step varied from 8 to 11.50 μm (Table 4), an indication that the objects discarded in this step tended to be of smaller size, where corrected sphericity is a shape descriptor of limited usefulness.

Despite of the selection of the second and third steps (Table 2), some elongated and flattened objects with spheroidal shape remained in the sample. These objects have shapes different than those expected and probably represent groups of a few of individuals. The filter applied during the fourth step (Table 2) discarded objects with mean sizes from 12.43 to 18.29 μm, tending to confirm this interpretation.

After applying these filters, spheroidal objects corresponding to groups of framboids, euhedrae or sunflowers or even to the infill of spheroidal holes in the carbonate matrix and foraminifera shells were selected (Figs. 8a and 8b). For this reason, the size distributions of populations of spheroidal groups were estimated during the SEM analysis.

Mixture of independent populations. The entire size distribution obtained after applying the four-step filtering process contains the mixture of independent populations corresponding to framboids, euhedrae or sunflowers. Moreover, spheroidal groups were also included in the entire size distribution. According to the law of proportionate effects, the growth rate of natural minerals is independent of their size and therefore crystal sizes follow lognormal distributions (Kile and Eberl 2003). Studies on the size distributions of framboidal and euhedral pyrite have shown that these have lognormal or quasi-lognormal shapes (Wilkin et al. 1996; Pósfai et al. 2001; Merinero et al. 2009). The SEM analysis of the studied carbonate pipes shows that populations of pyrite and iron oxyhydroxides by morphology and arrangement follow lognormal or quasi-lognormal distributions. Therefore, it can be assumed that the entire size distribution is made up of a mixture of several independent lognormal populations. With this criterion, the entire size distribution was separated into independent lognormal subpopulations using the Mclust function.

Correspondence between populations of the SEM and micro-CT analyses

During the SEM analysis, independent populations of pyrite and iron oxyhydroxides were characterized according to their morphology and arrangement. The size distributions of these lognormal or quasi-lognormal populations were estimated. The micro-CT analysis and the subsequent filtering process provided the entire size distribution containing the mixture of several independent and lognormal populations. These lognormal populations were characterized using the Mclust function. Correspondence between SEM and micro-CT populations was made based on the main parameters of the size distributions such as mean, standard deviation, minimum and maximum (Table 3). Micro-CT images and 3D renderings showing the arrangement and shape of the objects were also used to establish this correspondence (Fig. 8). The proposed correspondence between SEM and micro-CT populations can be observed in the rows of Table 3. In general, micro-CT populations have higher mean size than the corresponding SEM populations. For the standard deviation, there is no clear variation trend, although SEM populations of framboids have higher standard deviation than the corresponding micro-CT population.

These differences in the mean size can be explained by the techniques used in our study. During the SEM phase of the study, thin sections of the samples were used representing a random cut through objects that were not uniform in size. This introduces a measurement error that some authors estimate to be less than 10% (Wilkin et al. 1996; Cashman and Marsh 1988), although the error rate increases for objects of larger size due to the higher probability of large particle overlap in thin cross-sections (Castro et al. 2003). The resolution of micro-CT limits the minimum measurable size of the 3D objects to 4.33 μm. This also explains the smaller mean size of the SEM populations, mainly for the euhedral populations that have a smaller mean size.

Differences in the standard deviation can be explained by the representativeness of the micro-CT populations. SEM study is limited by the number of measured objects. Although measures of position such as the mean and the median can be estimated accurately with some hundreds of SEM observations (Wilkin et al. 1996), dispersion measures such as the standard deviation are more sensitive to the number of observations. Given the high number of objects measured during the micro-CT analysis (15000 on average) for each independent population, the estimation obtained for the standard deviation of the real populations can be considered as very reliable.

Pyrite and iron oxyhydroxides in the Cornide sample, and the Almazán inner and DIASOM inner samples show two different morphologies that have their corresponding populations in the micro-CT populations (Figs. 8c and 8d). In these samples, a third micro-CT population is obtained, related to spheroidal groups of sunflowers or framboids. Evidence for this can be found in the morphology of the 3D renderings for these populations (Fig. 8a). The filtering process applied to the entire size distribution allows differentiation of irregular and non-spheroidal objects, but some small groups of two or three objects with spheroidal shapes cannot be filtered. Moreover, SEM populations of spheroidal objects follow lognormal or quasi-lognormal distributions and this explains why the same kinds of populations under micro-CT analysis are also lognormal.

In all the samples studied, euhedral crystals have the smallest mean size (Table 3). The SEM populations of euhedrae in the Almazán outer sample and the first population of euhedrae in the DIASOM outer sample do not have a corresponding micro-CT population (Table 3). The size of the euhedrae in these populations is near or below the minimum size detected with micro-CT (4.33 µm), which explain this result. Moreover, the euhedral-2 and framboidal-2 populations in the Almazán outer sample form groups.

These objects can be separated into individual objects in the SEM study, but in the micro-CT analysis they are considered as groups of objects (Fig. 8b). This explains why they do not have a corresponding micro-CT population. In addition, the spherical groups of euhedrae and framboids are part of the micro-CT population and correspond to the population with the highest mean size.

The infilling of foraminiferal shells is very frequent in the DIASOM outer sample. Some of the chambers of the foraminiferal shells have a spheroidal shape and therefore they are not discriminated during the filtering process (Fig. 8b). This explains why the third micro-CT population is related to the infilling of foraminiferal shells.

Implications

This study finds a statistical procedure to obtain representative size distributions for different morphologies and arrangements of pyrite from SEM and micro-CT data.

The statistical procedure consisted in a first analysis using SEM data to obtain size distributions grouped by morphology and arrangement followed by a second analysis performed using micro-CT data, obtaining the size distributions of spheroidal and regular 3D objects. These size distributions were statistically analyzed to obtain the representative size distributions for each individual morphology and arrangement of pyrite.

Size distributions of pyrite were mainly used to infer paleo-environmental conditions of formation of framboids found in shales or limestones. Therefore, the statistical procedure described here can be applied to these sedimentary rocks containing framboidal pyrite. The high difference between the attenuation coefficients of the matrix of shales or limestones and pyrite, allows the use of micro-CT analysis to obtain the 3D volume of pyrite, on the assumption that minerals with similar attenuation coefficients than pyrite are scarce or not present in the studied rocks.

The problem of micro-CT analysis is that all occurrences of pyrite were considered in the 3D volume. The filtering process designed to select spherical and regular objects and the subsequent determination of the optimal mixture of lognormal size distributions allows representative size distributions to be obtained.

Previous studies determined size distributions of pyrite measuring the framboids in a 2D surface and extrapolating the results to the whole sample. These size distributions of pyrite had some limitations such as the lack of representativeness, the underestimation of the small sizes and the imprecision of measurement in random cuts through the microscopic pyrite, resulting in size distributions and inferences with possibly significant errors. The micro-CT analysis solves part of these problems obtaining representative size distributions and considering 3D morphologies rather than random cuts, but continues underestimating the lower sizes. The use of voxel sizes below 2.5 µm in future works will reduce this underestimation.

In the studied carbonate pipes, the mean, standard deviation and maximum sizes of most of the populations of framboids indicate formation within the first few centimeters of sediment below the oxic water-column. The population framboidal-1 occurring inside foraminiferal shells in the Hespérides sample has a size distribution that represents redox conditions near the threshold between oxic/dyoxic and euxinic regimes. Foraminiferal shells constitute isolated microenvironments where bacterial sulfate reduction takes place and therefore where framboidal pyrite forms and grows. Therefore, it is expected that foraminiferal shells represent different redox conditions than other open spaces where framboidal pyrite formed.

Acknowledgements

We would like to thank the Spanish Institute of Oceanography of Malaga for its contribution of samples for this study. We wish to thank Mr. Alfredo Larios (ICTS National Center for Electron Microscopy, Complutense University of Madrid) for his assistance with photomicrographs. Thanks to Ing. Pieter Vanderniepen (UGCT, Department of Physics and Astronomy, Ghent University) for his help and dedication on the performing micro-CT scans. Richard Wilkin and an anonymous reviewer are thanked for their constructive criticism and helpful comments in the revision of this manuscript. Victor Cárdenes also gratefully acknowledges to his Marie Curie IEF grant 623082 TOMOSLATE. This research was financed by the project SUBVENT-2 CGL2012-39524-C02-02 of the Spanish Ministry of Economy and Competitiveness.

References cited

Blood, D.R., and Lash, G.G. (2015) Dynamic redox conditions in the Marcellus Shale as recorded by pyrite framboid size distributions. The Geological Society of America Special Papers, 515, 153-168.

Bond, D.P., and Wignall, P.B. (2010) Pyrite framboid study of marine Permian–Triassic boundary sections: a complex anoxic event and its relationship to contemporaneous mass extinction. Geological Society of America Bulletin, 122, 1265-1279.

Brabant, L., Vlassenbroeck, J., De Witte, Y., Cnudde, V., Boone, M.N., Dewanckele, J. and Van Hoorebeke, L. (2011) Three-dimensional analysis of high-resolution X-ray computed tomography data with morpho+. Microscopy and Microanalysis, 17, 252-263.

Bribiesca, E. (2000) A measure of compactness for 3D shapes. Computers and Mathematics with Applications, 40, 1275-1284.

——— (2008) An easy measure of compactness for 2D and 3D shapes. Pattern Recognition, 41, 543-554.

Butler, I.B. and Rickard, D. (2000) Framboidal pyrite formation via the oxidation of iron (II) monosulfide by hydrogen sulphide. Geochimica et Cosmochimica Acta, 64, 2665-2672.

Cárdenes, V., Merinero, R., De Boever, W., Rubio-Ordóñez, A., Dewanckele, J., Cnudde, J.P., Boone, M., Van Hoorebeke, L. and Cnudde, V. (2016) Characterization of micropyrite populations in low-grade metamorphic slate: A study using high-resolution X-ray tomography. Palaeogeography, Palaeoclimatology, Palaeoecology, 441, 924-935.

Cashman, K.V., and Marsh, B. (1988) Crystal size distribution (CSD) in rocks and the kinetics and dynamics of crystallization II: Makaopuhi lava lake. Contributions to Mineralogy and Petrology, 99, 292-305.

Castro, J.M., Cashman, K.V., and Manga, M. (2003) A technique for measuring 3D crystal-size distributions of prismatic microlites in obsidian. American Mineralogist, 88, 1230-1240.

Cavalazzi, B., Barbieri, R., Cady, S.L., George, A.D., Gennaro, S., Westall, F., Lui, A., Canteri, R., Rossi, A.P., Ori, G.G. and Taj-Eddine, K. (2012) Iron-framboids in the hydrocarbon-related Middle Devonian Hollard Mound of the Anti-Atlas mountain range in Morocco: Evidence of potential microbial biosignatures. Sedimentary Geology, 263-264, 183-193.

Cnudde, V., and Boone, M.N. (2013) High-resolution X-ray computed tomography in geosciences: A review of the current technology and applications. Earth-Science Reviews, 123, 1-17.

Díaz-del-Río, V., Somoza, L., Martínez-Frías, J., Mata, M.P., Delgado, A., Hernández-Molina, F.J., Lunar, R., Martín-Rubí, J.A., Maestro, A., and others (2003). Vast fields of hydrocarbon-derived carbonate chimneys related to the accretionary wedge/olistostrome of the Gulf of Cádiz. Marine Geology, 195, 177-200.

Ding, H., Yao, S., and Chen, J. (2014) Authigenic pyrite formation and re-oxidation as an indicator of an unsteady-state redox sedimentary environment: Evidence from the intertidal mangrove sediments of Hainan Island, China. Continental Shelf Research, 78, 85-99.

Fraley, C., and Raftery, A.E. (2002) Model-based clustering, discriminant analysis, and density estimation. Journal of the American Statistical Association, 97, 611-631.

Fraley, C., Raftery, A.E., Murphy, T.B., and Scrucca, L. (2012) mclust Version 4 for R: Normal mixture modeling for model-based clustering, classification, and density estimation. Department of Statistics, University of Washington Technical Report, 597, 1-57.

Gallego-Torres, D., Reolid, M., Nieto-Moreno, V., and Martínez-Casado, F.J. (2015) Pyrite framboid size distribution as a record for relative variations in sedimentation rate: An example on the Toarcian Oceanic Anoxic Event in Southiberian Palaeomargin. Sedimentary Geology, 330, 59-73.

Guan, C., Zhou, C., Wang, W., Wan, B., Yuan, X., and Chen, Z. (2014) Fluctuation of shelf basin redox conditions in the early Ediacaran: Evidence from Lantian Formation black shales in South China. Precambrian Research, 245, 1-12.

Higgins, M.D. (2000) Measurement of crystal size distribution. American Mineralogist, 85, 1105-1116.

Kile, D.E., and Eberl, D.D. (2003) On the origin of size-dependent and size-independent crystal growth: Influence of advection and diffusion. American Mineralogist, 88, 1514-1521.

Large, D.J., Sawlowicz, Z., and Spratt, J. (1999) A cobaltite-framboidal pyrite association from the Kupferschiefer: possible implications for trace element behaviour during the earliest stages of diagenesis. Mineralogical Magazine, 63, 353-361.

Liao, W., Wang, Y., Kershaw, S., Weng, Z., and Yang, H. (2010) Shallow-marine dysoxia across the Permian–Triassic boundary: Evidence from pyrite framboids in the microbialite in South China. Sedimentary Geology, 232, 77-83.

Lindblad, J. (2005) Surface area estimation of digitized 3D objects using weighted local configurations. Image and Vision Computing, 23, 111-122.

Masschaele, B., Dierick, M., Van Loo, D., Boone, M.N., Brabant, L., Pauwels, E., Cnudde, V., and Van Hoorebeke, L. (2013) HECTOR: A 240 kV micro-CT setup optimized for research. Journal of Physics: Conference Series, 463, 012012.

Merinero, R., Lunar, R., Martínez-Frías, J., Somoza, L., and Díaz-del-Río, V. (2008) Iron oxyhydroxide and sulphide mineralization in hydrocarbon seep-related carbonate submarine chimneys, Gulf of Cadiz (SW Iberian Peninsula). Marine and Petroleum Geology, 25, 706-713.

Merinero, R., Lunar, R., Somoza, L., Díaz-del-Río, V., and Martínez-Frías, J. (2009) Nucleation, growth and oxidation of framboidal pyrite associated with hydrocarbon-derived submarine chimneys: lessons learned from the Gulf of Cadiz. European Journal of Mineralogy, 21, 947-961.

Montero, R.S., and Bribiesca, E. (2009) State of the art of compactness and circularity measures. International Mathematical Forum 4, 27, 1305-1335.

Ohfuji, H., and Rickard, D. (2005) Experimental syntheses of framboids—a review. Earth Science Reviews, 71, 147-170.

Ollion, J., Cochennec, J., Loll, F., Escudé, C., and Boudier, T. (2013) TANGO: a generic tool for high-throughput 3D image analysis for studying nuclear organization. Bioinformatics, 29, 1840-1841.

Peckmann, J., and Thiel, V. (2004) Carbon cycling at ancient methane–seeps. Chemical Geology, 205, 443-467.

Pósfai, M., Cziner, K., Márton, E., Márton, P., Buseck, P.R., Frankel, R.B., and Bazylinski, D.A. (2001) Crystal-size distributions and possible biogenic origin of Fe sulfides. European Journal of Mineralogy, 13, 691-703.

R_Core_Team (2015) R: A language and environment for statistical computing. Available: https://www.R-project.org/. R Foundation for Statistical Computing, Vienna.

Royston, P. (1995) Remark AS R94: A remark on Algorithm AS 181: The W-test for normality. Applied Statistics, 44, 547-551.

Rueda, J.L., Urra, J., Gofas, S., López-González, N., Fernández-Salas, L.M., and Díaz-del-Río, V. (2012) New records of recently described chemosymbiotic bivalves for mud volcanoes within the European waters (Gulf of Cádiz). Mediterranean Marine Science, 13/2, 262-267.

Sawlowicz, Z. (1993) Pyrite framboids and their development: a new conceptual mechanism. Geologische Rundschau, 82, 148-156.

Schneider, C.A., Rasband, W.S., and Eliceiri, K.W. (2012) NIH Image to ImageJ: 25 years of image analysis. Nature Methods, 9, 671-675.

Suits, N.S., and Wilkin, R.T. (1998) Pyrite formation in the water column and sediments of a meromictic lake. Geology, 26, 1099-1102.

Takahashi, S., Yamasaki, S.I., Ogawa, K., Kaiho, K., and Tsuchiya, N. (2015) Redox conditions in the end-Early Triassic Panthalassa. Palaeogeography, Palaeoclimatology, Palaeoecology, 432, 15-28.

Tian, L., Tong, J., Algeo, T.J., Song, H., Song, H., Chu, D., Shi, L., and Bottjer, D.J. (2014) Reconstruction of Early Triassic ocean redox conditions based on framboidal pyrite from the Nanpanjiang Basin, South China. Palaeogeography, Palaeoclimatology, Palaeoecology, 412, 68-79.

Vila, Y., Sobrino, I., and Jiménez, M.P. (2013) Fishery and life history of spot-tail mantis shrimp, *Squilla mantis* (Crustacea: Stomatopoda), in the Gulf of Cadiz (eastern central Atlantic). Scientia Marina, 77, 137-148.

Vlassenbroeck, J., Dierick, M., Masschaele, B., Cnudde, V., Van Hoorebeke, L., and Jacobs, P. (2007) Software tools for quantification of X-ray microtomography at the UGCT. Nuclear Instruments and Methods in Physics Research Section A: Accelerators, Spectrometers, Detectors and Associated Equipment, 580, 442-445.

Wadell, H. (1935) Volume, shape, and roundness of quartz particles. Journal of Geology, 43, 250-280.

Wang, P., Huang, Y., Wang, C., Feng, Z., and Huang, Q. (2013). Pyrite morphology in the first member of the Late Cretaceous Qingshankou formation, Songliao

Basin, northeast China. Palaeogeography, Palaeoclimatology, Palaeoecology, 385, 125-136.

Wei, H., Chen, D., Wang, J, Yu, H., and Tucker, M.E. (2012) Organic accumulation in the lower Chihsia Formation (Middle Permian) of South China: Constraints from pyrite morphology and multiple geochemical proxies. Palaeogeography, Palaeoclimatology, Palaeoecology, 353-355, 73-86.

Wei, H., Algeo, T.J., Yu, H., Wang, J., Guo, C., and Shi, G. (2015) Episodic euxinia in the Changhsingian (late Permian) of South China: Evidence from framboidal pyrite and geochemical data. Sedimentary Geology, 319, 78-97.

Wignall, P.B., Newton, R., and Brookfield, M.E. (2005) Pyrite framboid evidence for oxygen-poor deposition during the Permian–Triassic crisis in Kashmir. Palaeogeography, Palaeoclimatology, Palaeoecology, 216, 183-188.

Wilkin, R.T., Barnes, H.L., and Brantley, S.L. (1996) The size distribution of framboidal pyrite in modern sediments: an indicator of redox conditions. Geochimica et Cosmochimica Acta, 60, 3897-3912.

Tables

Table 1. Nomenclature of the samples used in this study, the complete sample identification, cruise and physiographic unit where samples were recovered.

Sample	Sample identification	Cruise	Physiographic unit
Cornide	ANAS-2001-DA02-MSN-N0016	Anastasya 2001	Cornide mud-volcano
Hespérides	CHICA0211-DA37-MSN-N0106	Chica 0211	Hespérides mud-volcano
Almazán outer	CHICA0211-BT26-MSN-N0107	Chica 0211	Almazán mud-volcano
Almazán inner	CHICA0211-BT26-MSN-N0107	Chica 0211	Almazán mud-volcano
DIASOM outer	ARSA0309-L34-MSN-N0101	Arsa 0309	DIASOM Field
DIASOM inner	ARSA0309-L34-MSN-N0101	Arsa 0309	DIASOM Field

Table 2. Four-step filtering process applied to the 3D objects obtained during the micro-CT analysis

Step	Filtering criteria	Objects filtered
Step 1	Adjust to the theoretical lognormal distribution in the smaller sizes	Noise
Step 2	Corrected sphericity less than 0.80	Non-spheroidal objects
Step 3	Discrete compactness less than 0.60	Non-spheroidal objects
Step 4	Elongation and flatness of the circumscribed 3D ellipsoid greater than 1.80 and the sum of the elongation and flatness greater than 3	Elongated and flattened objects

Table 3. Summary of the independent populations observed in the SEM analysis (left) and correspondence in the same row with lognormal populations obtained in the micro-CT analysis (right) for each sample. s.d. = standard deviation; min = minimum; max = maximum; %n = percentage in number of objects; %V = percentage in volume. n_{SEM} and $n_{micro\text{-}CT}$ are the number of objects measured in each analysis.

CORNIDE n_{SEM}=1639 $n_{micro\text{-}CT}$=34014													
		mean	**s.d.**	**min**	**max**			**%n**	**%V**	**mean**	**s.d.**	**min**	**max**
SEM	Euhedral	8.55	2.61	4.29	14.87	MCT	P1	36.31	4.92	9.32	2.22	4.33	14.61
	Sunflower	12.03	4.06	5.91	32.45		P2	39.15	25.53	16.18	4.24	8.89	33.25
	Sub-spherical groups	23.78	8.54	8.12	42.76		P3	24.53	69.56	24.91	9.06	12.02	147.57
							Total	100	100	15.15	9.19	4.33	147.57
HESPÉRIDES n_{SEM}=597 $n_{micro\text{-}CT}$=6874													
		mean	**s.d.**	**min**	**max**			**%n**	**%V**	**mean**	**s.d.**	**min**	**max**
SEM	Euhedral-1	4.96	1.61	2.80	10.32	MCT	P1	4.39	0.05	4.39	0.63	4.33	6.69
	Framboidal-1	6.93	2.55	4.30	11.92		P2	16.62	2.42	7.54	1.14	6.69	10.17
	Euhedral-2	8.38	1.26	5.66	11.17		P3	37.45	13.08	11.25	1.60	7.89	15.23
	Framboidal-2	12.05	3.29	5.04	19.03		P4	27.30	26.33	16.12	2.29	12.04	22.74
	Sunflower	18.41	13.46	3.76	50.46		P5	12.26	33.01	24.29	3.46	18.35	36.31
	Sub-spherical groups	22.95	9.59	10.03	40.54		P6	1.99	25.10	40.45	5.76	30.65	78.81
							Total	100	100	13.95	6.94	4.33	78.81
ALMAZÁN OUTER n_{SEM}=507 $n_{micro\text{-}CT}$=24906													
		mean	**s.d.**	**min**	**max**			**%n**	**%V**	**mean**	**s.d.**	**min**	**max**
SEM	Euhedral-1	2.96	0.46	2.14	3.99	MCT	P1	73.97	25.40	9.06	3.51	4.33	17.69
	Euhedral-2	4.64	0.39	4.13	5.21								
	Framboidal-1	7.55	1.97	2.47	13.82								
	Framboidal-2	11.61	3.80	5.46	18.00								
	Sub-spherical groups	22.85	16.07	4.30	101.28		P2	26	74.6	24.71	10.8	11.9	148.9
							Total	100	100	15.07	9.39	4.33	148.90
ALMAZÁN INNER n_{SEM}=500 $n_{micro\text{-}CT}$=9005													
		mean	**s.d.**	**min**	**max**			**%n**	**%V**	**mean**	**s.d.**	**min**	**max**
SEM	Euhedral	4.57	1.77	2.20	10.52	MCT	P1	31.70	4.29	7.59	2.30	4.33	11.89
	Framboidal	10.67	2.42	7.57	13.83		P2	32.28	14.98	11.98	3.20	6.43	21.70
	Sub-spherical groups	17.77	10.46	7.58	52.99		P3	36.01	80.73	18.25	9.37	8.42	103.82
							Total	100	100	12.95	7.57	4.33	103.82
DIASOM OUTER n_{SEM}=592 $n_{micro\text{-}CT}$=999													
		mean	**s.d.**	**min**	**max**			**%n**	**%V**	**mean**	**s.d.**	**min**	**max**
SEM	Euhedral-1	4.65	0.36	3.91	5.36	MCT							
	Euhedral-2	5.87	2.24	3.01	11.38		P1	7.68	0.25	5.50	1.49	4.33	7.62
	Framboidal	9.40	5.31	2.67	44.35		P2	50.07	9.98	10.86	2.93	5.57	19.08
	Sub-spherical groups	19.65	7.49	9.12	31.60		P3	35.18	36.92	19.67	5.31	11.37	39.38
	Foraminifera	24.99	4.67	16.69	32.24		P4	70.77	52.85	39.34	10.62	25.30	81.73
							Total	100	100	15.59	9.53	4.33	81.73
DIASOM INNER n_{SEM}=1790 $n_{micro\text{-}CT}$=15650													
		mean	**s.d.**	**min**	**max**			**%n**	**%V**	**mean**	**s.d.**	**min**	**max**
SEM	Euhedral	7.39	0.90	4.03	10.56	MCT	P1	16.20	1.82	6.47	2.12	4.33	9.51
	Sunflower	12.24	3.18	6.15	21.21		P2	63.22	37.67	11.65	3.82	5.57	26.77
	Sub-spherical groups	18.50	4.04	9.09	24.61		P3	20.58	60.52	20.54	6.74	12.16	76.45
							Total	100	100	12.65	6.37	4.33	76.45

Table 4. Summary of the four-step filtering process applied to 3D objects obtained during the micro-CT analysis. For each sample and step, the number (n), mean, standard deviation (s.d.), minimum (min) and maximum (max) sizes of the discarded objects were included.

	CORNIDE					**ALMAZÁN OUTER**					**DIASOM OUTER**				
	n	**mean**	**s.d.**	**min**	**max**	**n**	**mean**	**s.d.**	**min**	**max**	**n**	**mean**	**s.d.**	**min**	**max**
Initial	65693	17.98	22.72	2.5	933.09	35037	15.6	14.05	0	259.98	1400	15.62	11.69	2.5	108.39
Step 1	14322	5.39	0	4.33	7.38	2910	5.24	0	4.33	7.15	63	5.19	0	4.33	7.15
Step 2	3865	83.72	66.8	19.61	933.09	1964	63.45	31.85	20.02	259.98	65	48.95	18.39	25.54	108.39
Step 3	801	11.48	4.77	7.15	27.51	1587	8.01	3.12	5.95	16.61	40	8.4	3.69	5.95	15.88
Step 4	12601	18.29	15.35	5.57	116.17	3670	15.29	14.95	5.57	115.84	233	14.92	13.18	5.57	71
	HESPÉRIDES					**ALMAZÁN INNER**					**DIASOM INNER**				
	n	**mean**	**s.d.**	**min**	**max**	**n**	**mean**	**s.d.**	**min**	**max**	**n**	**mean**	**s.d.**	**min**	**max**
Initial	10235	17.41	23.08	2.5	895.7	13399	12.88	11.84	2.5	302.24	31894	14.13	16.27	2.5	771.33
Step 1	1510	5.15	0	4.33	7.15	1672	5.13	0	4.33	7.15	4808	5.26	0	4.33	7.26
Step 2	344	103.6	70.24	24.8	895.7	1258	56.2	35.15	18.31	302.24	3204	50.39	37.76	11.12	771.33
Step 3	49	8.59	3.63	7.14	23.3	458	9.3	4.32	5.95	22.99	2028	11.35	4.14	5.95	30.95
Step 4	1458	15.26	15.38	5.57	108.51	1006	12.43	12.59	5.57	98.59	6204	13.10	10.48	5.57	92.24

Figure Captions

Figure 1. Photographs and transversal and longitudinal sections of the carbonate pipes from the Gulf of Cadiz studied here: (**a**) and (**b**) Cornide; (**c**) and (**d**) Hespérides; (**e**) and (**f**) Almazán; (**g**) and (**h**) DIASOM.

Figure 2. Thin-section back-scatter SEM photomicrographs showing the three morphologies of pyrite and iron oxyhydroxides in the studied samples: (**a**) framboids, (**b**) euhedrae (**c**) sunflowers.

Figure 3. Thin-section back-scatter SEM photomicrographs showing the morphologies and arrangements of pyrite and iron oxyhydroxides in: (**a**), (**b**) and (**c**) Cornide; (**d**), (**e**) and (**f**) Hespérides; (**g**), (**h**) and (**i**) Almazán Outer.

Figure 4. Thin-section back-scatter SEM photomicrographs showing the morphologies and arrangements of pyrite and iron oxyhydroxides in: (**a**), (**b**) and (**c**) Almazán Inner; (**d**), (**e**) and (**f**) DIASOM Outer; (**g**), (**h**) and (**i**) DIASOM Inner.

Figure 5. Histograms and quantile-quantile plots of independent populations observed in the SEM analysis. The theoretical lognormal distribution was included in the histograms and the result of the Shapiro-Wilk test (Royston, 1995) in the quantile-quantile plot. (**a**) euhedrae and (**b**) spheroidal groups in the Cornide sample; (**c**) framboids and (**d**) spheroidal groups of framboids in the Hespérides sample; (**e**) sunflowers and (**f**) spheroidal groups of sunflowers in the DIASOM Inner sample.

Figure 6. Histograms of the entire size distribution obtained during the micro-CT analysis for each sample. The probability density functions of the lognormal subpopulations obtained during the mixture analysis were plotted in different colors.

Figure 7. Attenuation coefficient for pyrite, iron oxyhydroxides and main (dashed) and accessory (dotted) minerals in the samples studied, in relation to the energy of the X-ray

beam. Values are calculated taking into account the chemical composition of the minerals. Data obtained from the Physical Measurement Laboratory, National Institute of Standards and Technology (physics.nist.gov).

Figure 8. High-resolution X-ray tomography photomicrographs and 3D renderings produced with the plugin RoiManager3D 2.0 for ImageJ: (**a**) and (**b**) spheroidal groups of framboids in the Cornide sample; (**c**) and (**d**) spheroidal foraminifera infilling in the DIASOM Outer sample; (**e**) and (**f**) euhedrae in the DIASOM Inner sample; (**g**) and (**h**) sunflowers in the Hespérides sample. In red objects selected within the threshold of the grey scale; in yellow, objects selected after applying the filtering process and corresponding to the shape and size of the 3D renderings.

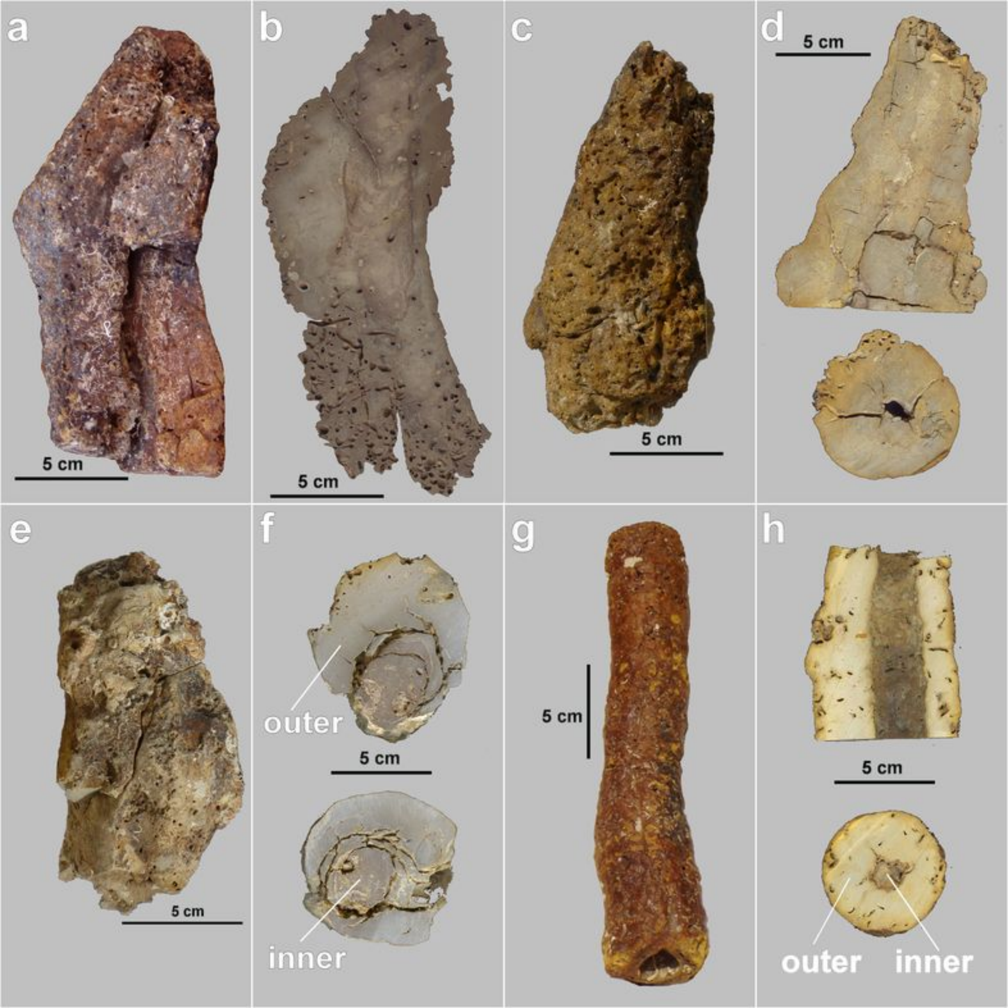
a
5 cm
b
5 cm
c
5 cm
d
5 cm
e
5 cm
f
outer
5 cm
inner
g
5 cm
h
5 cm
outer
inner

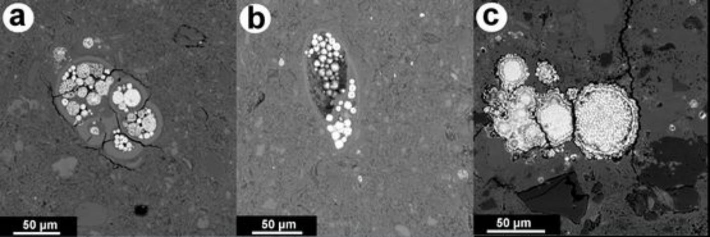
a
50 μm
b
50 μm
c
50 μm

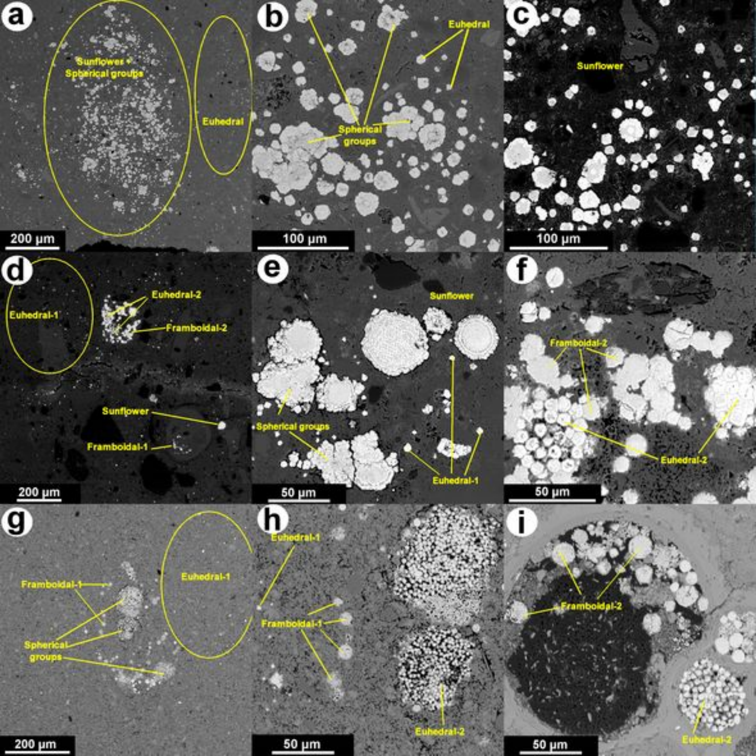
a
Sunflowers + Spherical groups
Euhedral
200 μm
b
Euhedral
Spherical groups
100 μm
c
Sunflower
100 μm
d
Euhedral-1
Euhedral-2
Framboidal-2
Sunflower
Framboidal-1
200 μm
e
Sunflower
Spherical groups
Euhedral-1
50 μm
f
Framboidal-2
Euhedral-2
50 μm
g
Framboidal-1
Euhedral-1
Spherical groups
200 μm
h
Euhedral-1
Framboidal-1
Euhedral-2
50 μm
i
Framboidal-2
Euhedral-2
50 μm

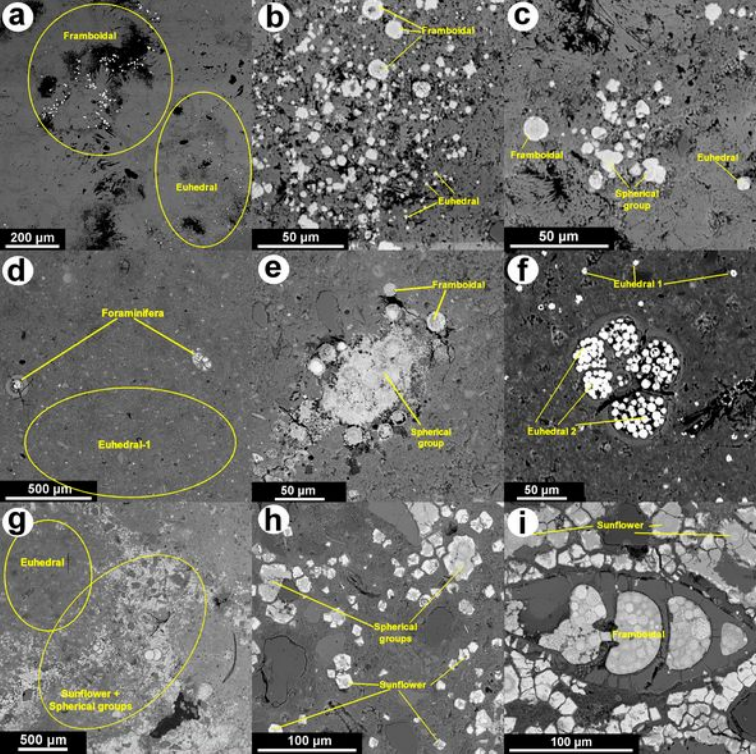
a
Framboidal
Euhedral
200 µm
b
Framboidal
Euhedral
50 µm
c
Framboidal
Spherical group
Euhedral
50 µm
d
Foraminifera
Euhedral-1
500 µm
e
Framboidal
Spherical group
50 µm
f
Euhedral 1
Euhedral 2
50 µm
g
Euhedral
Sunflower + Spherical groups
500 µm
h
Spherical groups
Sunflower
100 µm
i
Sunflower
Framboidal
100 µm

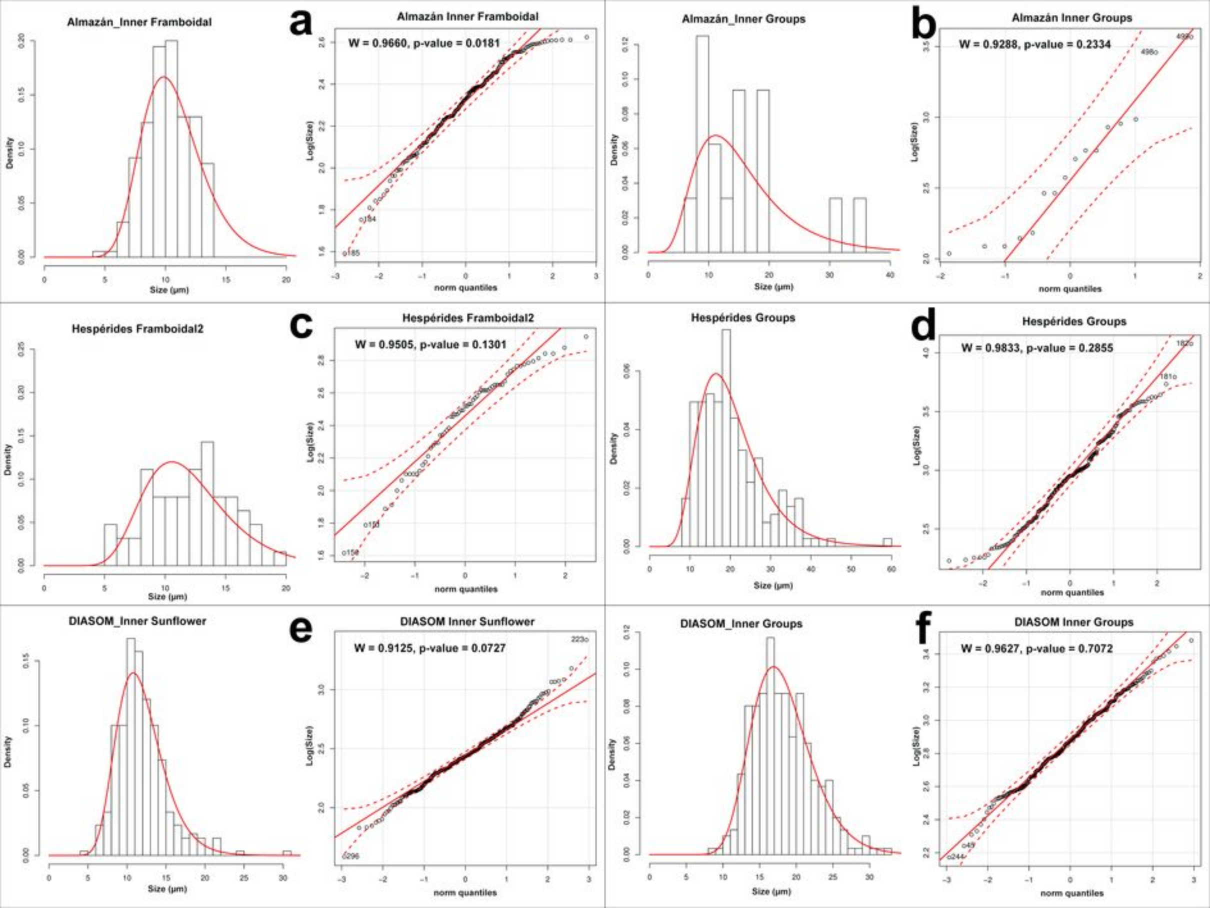

Almazán_Inner Framboidal
Density
Size (µm)
a
Almazán Inner Framboidal
W = 0.9660, p-value = 0.0181
Log(Size)
norm quantiles
184
185
Almazán_Inner Groups
Density
Size (µm)
b
Almazán Inner Groups
W = 0.9288, p-value = 0.2334
Log(Size)
norm quantiles
498
499
Hespérides Framboidal2
Density
Size (µm)
c
Hespérides Framboidal2
W = 0.9505, p-value = 0.1301
Log(Size)
norm quantiles
150
158
Hespérides Groups
Density
Size (µm)
d
Hespérides Groups
W = 0.9833, p-value = 0.2855
Log(Size)
norm quantiles
182
181
DIASOM_Inner Sunflower
Density
Size (µm)
e
DIASOM Inner Sunflower
W = 0.9125, p-value = 0.0727
Log(Size)
norm quantiles
223
296
DIASOM_Inner Groups
Density
Size (µm)
f
DIASOM Inner Groups
W = 0.9627, p-value = 0.7072
Log(Size)
norm quantiles
49
244

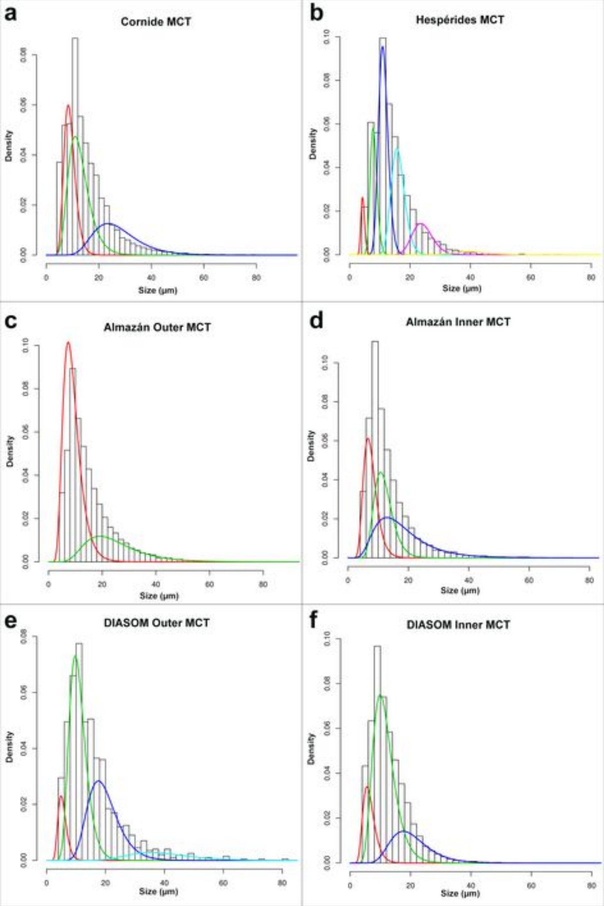
a
Cornide MCT
Density
0.00
0.02
0.04
0.06
0.08
0
20
40
60
80
Size (µm)
b
Hespérides MCT
Density
0.00
0.02
0.04
0.06
0.08
0.10
0
20
40
60
80
Size (µm)
c
Almazán Outer MCT
Density
0.00
0.02
0.04
0.06
0.08
0.10
0
20
40
60
80
Size (µm)
d
Almazán Inner MCT
Density
0.00
0.02
0.04
0.06
0.08
0.10
0
20
40
60
80
Size (µm)
e
DIASOM Outer MCT
Density
0.00
0.02
0.04
0.06
0.08
0
20
40
60
80
Size (µm)
f
DIASOM Inner MCT
Density
0.00
0.02
0.04
0.06
0.08
0.10
0
20
40
60
80
Size (µm)

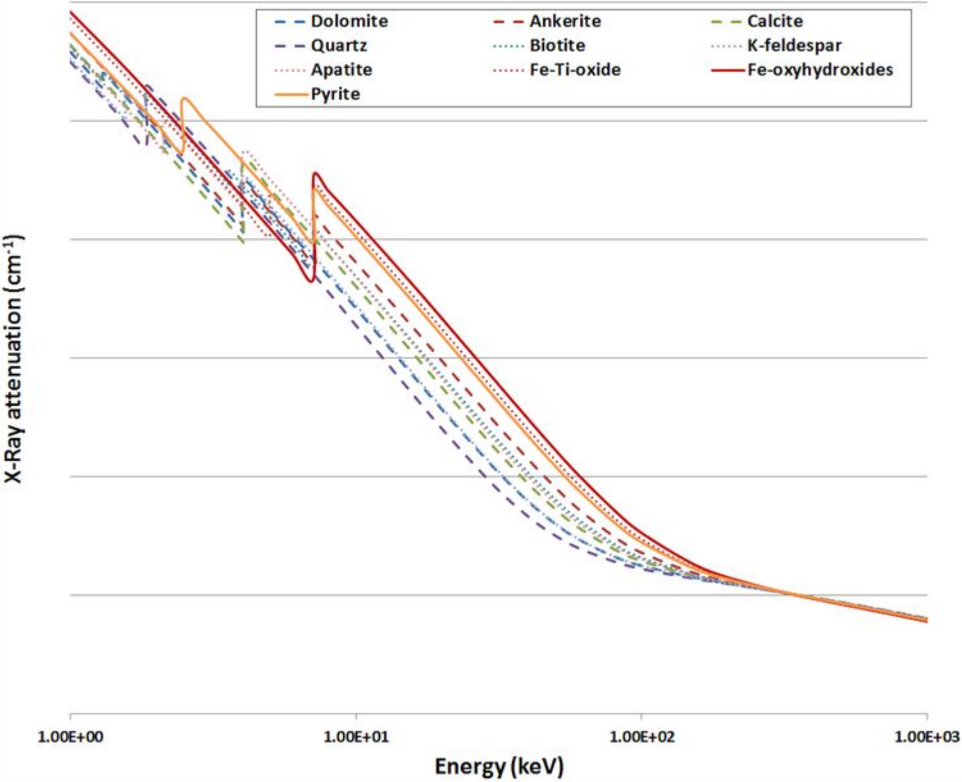
Dolomite
Ankerite
Calcite
Quartz
Biotite
K-feldespar
Apatite
Fe-Ti-oxide
Fe-oxyhydroxides
Pyrite
X-Ray attenuation (cm-1)
1.00E+00
1.00E+01
1.00E+02
1.00E+03
Energy (keV)

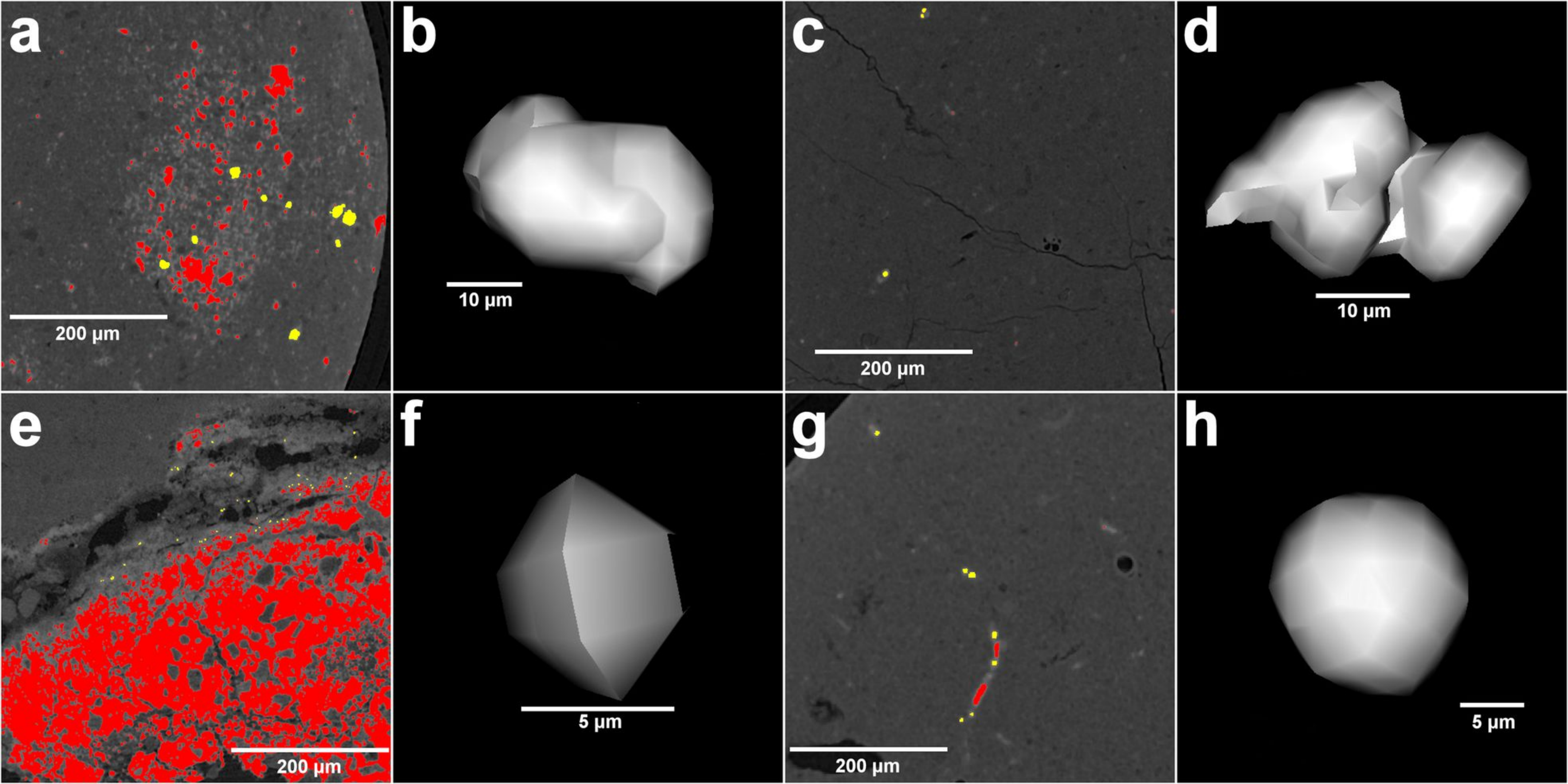
a
200 µm
b
10 µm
c
200 µm
d
10 µm
e
200 µm
f
5 µm
g
200 µm
h
5 µm